Delft University of Technology

Simplified Quadratic Optimization based IPMSM Full-Speed Range Rotor Position Estimation in Synchronous Rotating Frame

Peng, Fei; Cao, Zhi; Dong, Jianning; Huang, Yunkai

Citation (APA)
Peng, F., Cao, Z., Dong, J., & Huang, Y. (2021). Simplified Quadratic Optimization based IPMSM Full-Speed Range Rotor Position Estimation in Synchronous Rotating Frame. *IEEE Transactions on Transportation Electrification* , *7*(3), 1527 - 1536. Article 9349110. https://doi.org/10.1109/TTE.2021.3057491

Important note
To cite this publication, please use the final published version (if applicable).
Please check the document version above.

Simplified Quadratic Optimization-Based IPMSM Full-Speed Range Rotor Position Estimation in Synchronous Rotating Frame

Fei Peng, *Member, IEEE*, Zhi Cao, *Student Member, IEEE*, Jianning Dong, *Member, IEEE*, and Yunkai Huang, *Member, IEEE*

Abstract—This article proposes a rotor position and speed estimation method for the interior permanent magnet synchronous machine (IPMSM) in the full-speed range. The proposed method is implemented in the synchronous rotating frame. Based on the voltage equation of the IPMSM in the synchronous rotating frame, a single-variable optimization problem is formulated to solve the rotor position at each current sampling step. After that, the solved position is fed into a phase-locked loop observer to obtain the estimated rotor speed and smooth out the estimation. The proposed position and speed estimation methods are effective from standstill to high speed, and no estimation algorithm switching is needed during speed variation. Details about the convexity of the optimization problem, the effects of parameter mismatch and sampling noise, and the solving method of the problem are discussed. Finally, experiments are conducted in both steady and dynamic situations to validate the effectiveness and robustness of the proposed algorithm.

Index Terms—Full-speed range, interior permanent magnet synchronous machine (IPMSM), optimization problem, position sensorless control.

I. INTRODUCTION

THE interior permanent magnet synchronous machine (IPMSM) is widely used as a traction motor because of its high power density and wide speed range. To drive the IPMSM, the signal of rotor position is needed. The rotor position signal is often obtained from a position sensor mounted on the shaft. However, in typical applications requiring high reliability, e.g., traction, the position sensor may fail as a result of mechanical or environmental issues. Therefore, a fallback position estimation method independent of the shaft-mounted sensor can be used. The estimated position can be used for status diagnosis during normal operation. In the case of a position sensor failure, a transition between the sensed position and the estimated one will be carried out to keep the drive running [1].

The IPMSM rotor position estimation algorithm can be classified into two different categories. One is usable for the estimation at medium or high speed, while the other one is able to estimate at low or zero speed.

The back-electromotive force (Back EMF) is a good indicator of the rotor position. Therefore, the extended Back EMF method is widely used to detect the rotor position at medium to high speeds. First, based on the voltage equations of IPMSM, the extended Back EMF is derived. A couple of methods are available for the Back EMF estimation. Among them, Kalman filter methods [2], model reference adaptive methods [3], and observer methods [4], [5] are the most commonly used. The position of the rotor is then obtained from the estimated Back EMF. However, the Back EMF is proportional to the motor speed. When the motor runs at low speed, the Back EMF is small and difficult to be estimated. Therefore, this category of methods is only effective when the rotor speed is sufficiently high.

At zero to low speed, saliency-based methods are the standard approach for position estimation of IPMSM. The stator inductance of the IPMSM is a function of rotor position. High-frequency current or voltage signals are injected into the stator to estimate the stator inductance [6]–[17]. Since the pulsewidth modulation (PWM) voltage and its corresponding current ripple have high-frequency components, they are also sampled and taken as high-frequency signals [18]–[23]. However, this category of position estimation methods uses high- or low-pass filters for signal processing. As a consequence, they usually have limited dynamic response, and the injected signal has to be carefully selected. Moreover, the injected high-frequency signal causes acoustic noise and additional power losses. Therefore, this kind of methods is often used at low speed only.

The two categories of position estimation method are often adopted together to estimate the IPMSM rotor position in the full-speed range [1], [13], [24]. Therefore, a switching method is needed when the motor speed varies between low and high. In the traction application, the motor speed varies very often; therefore, the two position estimation methods have to be frequently switched from each other. The implementation and the estimation method switching increase the control system complexity. Since both methods need initialization, the transition between the two methods has to be carefully implemented. Frequent switching between the estimation methods may also result in unwanted oscillations in the position and speed estimations.

Unified position estimation methods have been proposed to tackle the aforementioned method switching problem for IPMSM control in the full-speed range [23], [25]–[29]. These methods utilize a unified voltage model [23], [27], [28] or flux model [25], [26] in the full-speed range. No estimation method switching is needed during speed variation. In [25], a flux observer is designed to observe the rotor flux, only the difference between the estimated rotor flux and the known permanent magnet (PM) flux is fed back to correct the estimation, the estimation accuracy is limited. In [26], the flux observer is designed in a quadratic form, and more prior knowledge and limits are applied; therefore, the estimation results are more accurate. However, there are several high- and low-pass filters involved in the estimation, which makes the design complicated. In [23] and [27], the position estimation is interpreted as a multivariable quadratic optimization problem. The rotor position and speed are estimated simultaneously from the solution of the optimization problem. However, the solving process is complex and time-consuming. Wang *et al.* [24] and Peng *et al.* [25] propose a method to simplify the process to solve the optimization problem in the stationary frame. The rotor position is obtained at first from the solution. Then, a conventional phase-locked loop (PLL) observer is adopted to obtain the speed. The computation demand is reduced. Since the derivation and solving process are performed in the stationary frame, therefore, this method is quite straightforward. However, several trigonometric function computations are needed while solving the estimated position, which increases its computation time.

Based on the previous work presented in [28] and [29], this article proposes an improved position estimation method for IPMSM using simplified quadratic optimization in the full-speed range. The proposed method also interprets the position estimation as a single-variable optimization problem. However, to further clarify the derivation and simplify the solving process, the optimization problem is formulated based on the IPMSM voltage equations in the synchronous rotating frame. Moreover, after applying the Taylor expansion on the voltage equation in the synchronous rotating frame, the convexity of the problem, the sampling noise, and parameter sensitivity are more straightforward to analyze, and the solving method is also remarkably simplified compared to the similar method presented in [23] and [27]–[29]. In the end, both the effectiveness and the robustness of the proposed method are validated on a traction motor.

II. IPMSM MODEL IN SYNCHRONOUS ROTATING FRAME

The IPMSM model is first derived as differential equations in the estimated rotating frame. If the rotor position is accurately known, then IPMSM voltage equation in the rotating dq frame is expressed as

$$
\begin{bmatrix} u_d \\ u_q \end{bmatrix} = \begin{bmatrix} R_s & -\omega_e L_q \\ \omega_e L_d & R_s \end{bmatrix} \begin{bmatrix} i_d \\ i_q \end{bmatrix} \\
+ \begin{bmatrix} L_d & 0 \\ 0 & L_q \end{bmatrix} \frac{d}{dt} \begin{bmatrix} i_d \\ i_q \end{bmatrix} + \psi_f \omega_e \begin{bmatrix} 0 \\ 1 \end{bmatrix} \quad (1)
$$

where i_d, i_q and u_d, u_q are the currents and voltages in the dq frame, respectively. R_s represents the stator resistance.

L_d and L_q are the dq-axis stator inductances. ω_e is the electrical angular speed of the rotor. ψ_f is the stator flux linkage from the PM.

Assuming that an estimated frame is rotating at the same speed as the dq frame, the angle between them is

$$
\tilde{\theta} = \theta_e - \hat{\theta} \quad (2)
$$

where θ_e is the electrical position of the real d-axis with respect to phase a, while $\hat{\theta}$ is that of the estimated frame. In the estimated frame, the voltage equation is derived as

$$
\begin{bmatrix} \hat{u}_d \\ \hat{u}_q \end{bmatrix} = \begin{bmatrix} R_s & -\omega_e L_1 \\ \omega_e L_1 & R_s \end{bmatrix} \begin{bmatrix} \hat{i}_d \\ \hat{i}_q \end{bmatrix} + \begin{bmatrix} L_1 & 0 \\ 0 & L_1 \end{bmatrix} \frac{d}{dt} \begin{bmatrix} \hat{i}_d \\ \hat{i}_q \end{bmatrix} \\
+ \psi_f \omega_e \begin{bmatrix} -\sin(\tilde{\theta}) \\ \cos(\tilde{\theta}) \end{bmatrix} \\
+ L_a(\tilde{\theta}) \frac{d}{dt} \begin{bmatrix} \hat{i}_d \\ \hat{i}_q \end{bmatrix} + \omega_e L_b(\tilde{\theta}) \begin{bmatrix} \hat{i}_d \\ \hat{i}_q \end{bmatrix} \quad (3)
$$

where $\hat{i}_d$, $\hat{i}_q$ and $\hat{u}_d$, $\hat{u}_q$ are the currents and voltages in the estimated frame, respectively. $L_a(\tilde{\theta})$ and $L_b(\tilde{\theta})$ are defined as

$$
L_a(\tilde{\theta}) = L_2 \begin{bmatrix} \cos(2\tilde{\theta}) & \sin(2\tilde{\theta}) \\ \sin(2\tilde{\theta}) & -\cos(2\tilde{\theta}) \end{bmatrix} \\
L_b(\tilde{\theta}) = L_2 \begin{bmatrix} -\sin(2\tilde{\theta}) & \cos(2\tilde{\theta}) \\ \cos(2\tilde{\theta}) & \sin(2\tilde{\theta}) \end{bmatrix}. \quad (4)
$$

L_1 and L_2 are defined as

$$
L_1 = \frac{L_d + L_q}{2} \\
L_2 = \frac{L_d - L_q}{2}. \quad (5)
$$

Equation (3) is then discretized for digital implementation

$$
\begin{bmatrix} \hat{u}_d(k) \\ \hat{u}_q(k) \end{bmatrix} = \begin{bmatrix} R_s & -\omega_e L_1 \\ \omega_e L_1 & R_s \end{bmatrix} \begin{bmatrix} \hat{i}_d(k) \\ \hat{i}_q(k) \end{bmatrix} + L_1 \frac{\Delta \hat{i}_{dq}(k)}{T} \\
+ \psi_f \omega_e \begin{bmatrix} -\sin(\tilde{\theta}(k)) \\ \cos(\tilde{\theta}(k)) \end{bmatrix} \\
+ L_a(\tilde{\theta}(k)) \frac{\Delta \hat{i}_{dq}(k)}{T} + \omega_e L_b(\tilde{\theta}(k)) \begin{bmatrix} \hat{i}_d(k) \\ \hat{i}_q(k) \end{bmatrix} \quad (6)
$$

where k is the time step and T denotes the sampling period. $L_a(\tilde{\theta}(k))$ and $L_b(\tilde{\theta}(k))$ are defined as

$$
L_a(\tilde{\theta}(k)) = L_2 \begin{bmatrix} \cos(2\tilde{\theta}(k)) & \sin(2\tilde{\theta}(k)) \\ \sin(2\tilde{\theta}(k)) & -\cos(2\tilde{\theta}(k)) \end{bmatrix} \\
L_b(\tilde{\theta}(k)) = L_2 \begin{bmatrix} -\sin(2\tilde{\theta}(k)) & \cos(2\tilde{\theta}(k)) \\ \cos(2\tilde{\theta}(k)) & \sin(2\tilde{\theta}(k)) \end{bmatrix}. \quad (7)
$$

$\Delta \hat{i}_{dq}(k)$ is defined as

$$
\Delta \hat{i}_{dq}(k) = \begin{bmatrix} \hat{i}_d(k) \\ \hat{i}_q(k) \end{bmatrix} - \begin{bmatrix} \hat{i}_d(k-1) \\ \hat{i}_q(k-1) \end{bmatrix}. \quad (8)
$$

III. PROPOSED QUADRATIC OPTIMIZATION-BASED ESTIMATION METHOD

The optimization problem to solve the rotor position is implemented based on (6) since it is effective in the full-speed range. The optimization problem can be formulated as the minimization of a cost function. After solving the optimization
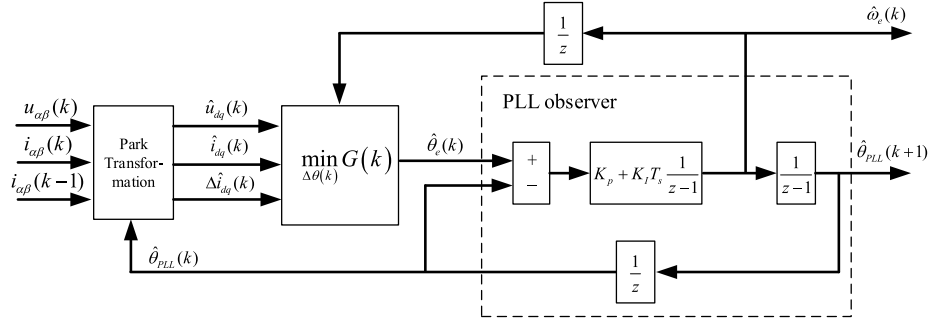
Fig. 1. Block diagram of the proposed improved rotor position and speed estimation method based on quadratic optimization in the synchronous rotating frame.

problem, the obtained result is fed into a PLL observer to filter out the high-frequency noise and obtain the rotor speed. The convexity of the cost function, the sensitivity of the method on sampling noise, and parameter mismatches are analyzed in detail. The high-frequency signal required at zero and low speed is also discussed. In the end, the solving method of the optimization problem is presented.

A. Proposed Simplified Quadratic Optimization for Position Estimation

It is observed from (6) that the first two terms do not contain $\tilde{\theta}$, while the last three terms are related to $\tilde{\theta}$. Then, the position estimation problem is transformed to solving the correct $\tilde{\theta}$ so that (6) can hold. However, there are two dimensions in (6), while only one variable has to be solved. Therefore, a quadratic optimization problem is formed so that the optimal $\tilde{\theta}$ in the least-squares sense is obtained in the end. First, in order to separate the terms that have no relationship with $\tilde{\theta}$, define an intermediate variable as

$$\begin{bmatrix} e_d(k) \\ e_q(k) \end{bmatrix} = \begin{bmatrix} \hat{u}_d(k) \\ \hat{u}_q(k) \end{bmatrix} - \begin{bmatrix} R_s & -\omega_e L_1 \\ \omega_e L_1 & R_s \end{bmatrix} \begin{bmatrix} \hat{i}_d(k) \\ \hat{i}_q(k) \end{bmatrix} - L_1 \frac{\Delta \hat{i}_{dq}(k)}{T}. \quad (9)$$

Then, the quadratic cost function $G(k)$ is defined as

$$F(k) = \begin{bmatrix} e_d(k) \\ e_q(k) \end{bmatrix} - \psi_f \omega_e \begin{bmatrix} -\sin(\Delta\theta(k)) \\ \cos(\Delta\theta(k)) \end{bmatrix}$$
$$- L_a(\Delta\theta(k)) \frac{\Delta \hat{i}_{dq}(k)}{T} - \omega_e L_b(\Delta\theta(k)) \begin{bmatrix} \hat{i}_d(k) \\ \hat{i}_q(k) \end{bmatrix}$$
$$G(k) = F(k)^T F(k) \quad (10)$$

where $\Delta\theta(k)$ is a variable. The optimization problem is formulated as

$$\min_{\Delta\theta(k)} G(k). \quad (11)$$

Ideally, the solution for $\Delta\theta(k)$ is $\tilde{\theta}(k)$, and in that case, $G(k) = 0$. Nevertheless, the factors of sampling noise, parameter mismatch, and speed estimation error will prevent $G(k)$ from reaching zero. The effect of these factors will be discussed afterward. After obtaining the optimal $\Delta\theta(k)$,

according to (2), the estimated rotor position at time k could calculated by

$$\hat{\theta}_e(k) = \hat{\theta}(k) + \Delta\theta(k). \quad (12)$$

In (10), ω_e is needed for calculation; however, it is not available from measurement. After obtaining the estimated position $\hat{\theta}_e(k)$, a regular PLL observer is used to estimate ω_e and gives out the initial value for solving the optimization problem, as shown in Fig. 1. The PLL observer used in this article is the same as that used in [29], from where more details could be found.

B. Convexity Examination of the Cost Function

In order to guarantee the solvability of the optimization problem presented by (11), the cost function (10) has to be at least locally convex. Therefore, its convexity has to be examined.

1) Standstill: At standstill, the term with ω_e in (10) becomes 0. It is then reformulated as

$$F(k) = \begin{bmatrix} e_d(k) \\ e_q(k) \end{bmatrix} - L_a(\Delta\theta(k)) \frac{\Delta \hat{i}_{dq}(k)}{T}$$
$$G(k) = F(k)^T F(k). \quad (13)$$

Substituting (6) and (9) into (13), there is

$$G(k) = \begin{bmatrix} e_d(k) \\ e_q(k) \end{bmatrix}^T \begin{bmatrix} e_d(k) \\ e_q(k) \end{bmatrix}$$
$$+ 4 L_2^2 \frac{\Delta \hat{i}_{dq}(k)^T \Delta \hat{i}_{dq}(k)}{T^2} \left(\sin\left(\Delta\theta(k) - \tilde{\theta}(k)\right) \right)^2. \quad (14)$$

It can be seen that if $\Delta \hat{i}_{dq}(k) = 0$, $G(k)$ remains constant, which makes the optimization problem unsolvable. If $\Delta \hat{i}_{dq}(k) \neq 0$, $G(k)$ becomes a periodical function with a period of π. $G(k)$ is locally convex within $[-\pi/2, \pi/2]$. The optimal solution that minimizes $G(k)$ is $\Delta\theta(k) = \tilde{\theta}(k)$. To keep $\Delta i_{dq}(k) \neq 0$, either high-frequency voltage or high-frequency current signal has to be added on the stator current.

Since $G(k)$ is only locally convex, in the iteration process, the initial value of $\Delta\theta(k)$ should be in the range of $\tilde{\theta}(k) \pm \pi/2$. If not, the solution of $\Delta\theta(k)$ will be π away from $\tilde{\theta}(k)$. The desired initial value of $\Delta\theta(k)$ is obtained by determining the polarity at startup.
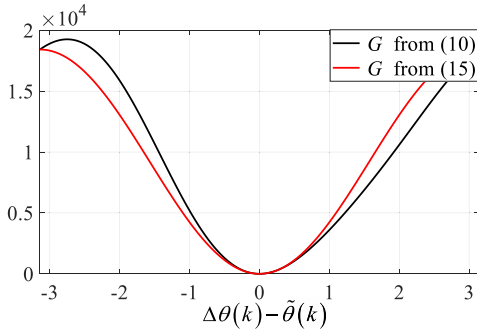
Fig. 2.   Waveforms of $G(k)$ with $\tilde{\theta}(k)$ being $\pi/2$ rad at rated speed.
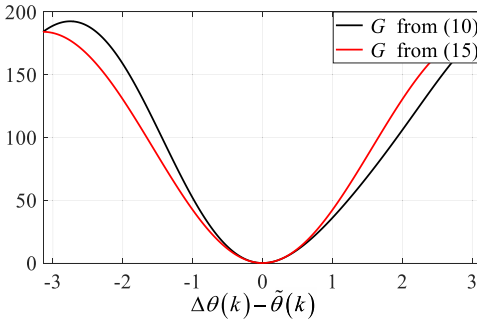

Fig. 3.   Waveforms of $G(k)$ with $\tilde{\theta}(k)$ being $\pi/2$ rad at 1/10 rated speed.

2) Medium and High Speeds: At medium to high speeds, the back EMF term will dominate in (10). The voltage drop caused by L_2 is usually small. Therefore, to simplify the analysis, the terms associated with L_2 are neglected in this situation. Then, $G(k)$ could be rewritten as

$$G(k) \approx 4{\psi_f}^2{\omega_e}^2\left(\sin\left(\frac{\Delta\theta(k) - \tilde{\theta}(k)}{2}\right)\right)^2. \tag{15}$$

It can be derived from (15) that the period of $G(k)$ is 2π and is convex between $[-\pi, \pi]$. Therefore, the optimization function could be solved, and the solution is unique.

To validate the analysis above, Figs. 2 and 3 show the waveforms of $G(k)$ with respect to $\Delta\theta(k) - \tilde{\theta}(k)$ obtained from (15) and (10), respectively, at the rated speed and 1/10 of the rated speed, with the rated current. The difference introduced by neglecting the terms associated with L_2 is observable, but it is small. Thus, the approximation of (15) is reasonable. The waveforms of (10) are all convex in the range $[-\pi, \pi]$, even at different speed. It is also shown that the slope of $G(k)$ increases with the speed. A higher slope indicates stronger robustness against sampling noise in real applications.

3) Low Speed: At low speed, none of the terms in (10) is small enough to be negligible compared to others. This makes the analysis more complex. To make the analysis possible, $F(k)$ is expanded into the Taylor series at $\tilde{\theta}(k)$, and then, $G(k)$ becomes

$$G(k) = \left\| A\left(\tilde{\theta}(k)\right) \right\|^2 \left(\Delta\theta(k) - \tilde{\theta}(k)\right)^2 \tag{16}$$
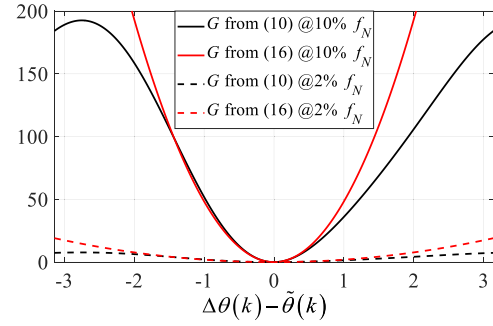

Fig. 4.   Waveforms of $G(k)$ with $\tilde{\theta}(k)$ being $\pi/2$ rad at 1/10 and 1/50 of the rated speed, where f_N is the rated motor rotating frequency.

where $\left\| A(\tilde{\theta}(k)) \right\|^2$ is the slope of $G(k)$

$$
\begin{aligned}
& A\left(\tilde{\theta}(k)\right) \\
& = 2\omega_e L_2 \begin{bmatrix} \cos\left(2\tilde{\theta}(k)\right) & \sin\left(2\tilde{\theta}(k)\right) \\ \sin\left(2\tilde{\theta}(k)\right) & -\cos\left(2\tilde{\theta}(k)\right) \end{bmatrix} \begin{bmatrix} \hat{i}_d \\ \hat{i}_q \end{bmatrix} \\
& \quad + 2L_2 \begin{bmatrix} \sin\left(2\tilde{\theta}(k)\right) & -\cos\left(2\tilde{\theta}(k)\right) \\ -\cos\left(2\tilde{\theta}(k)\right) & -\sin\left(2\tilde{\theta}(k)\right) \end{bmatrix} \frac{\Delta\hat{i}_{dq}(k)}{T} \\
& \quad + \omega_e \psi_f \begin{bmatrix} \cos\left(\tilde{\theta}(k)\right) \\ \sin\left(\tilde{\theta}(k)\right) \end{bmatrix}.
\end{aligned} \tag{17}
$$

To validate the approximation method above, the waveforms of $G(k)$ with respect to $\Delta\theta(k) - \tilde{\theta}(k)$ are calculated from both (10) and (16) at 1/10 and 1/50 of the rated speed, respectively. Fig. 4 compares the waveforms obtained from the two equations. Both (16) and Fig. 4 indicate that $G(k)$ is at least locally convex when $\Delta\theta(k) - \tilde{\theta}(k)$ is near zero and $\left\| A(\tilde{\theta}(k)) \right\| \neq 0$. Therefore, (11) is solvable, and the correct estimation result could be obtained if the two conditions are met: 1) $\left\| A(\tilde{\theta}(k)) \right\| > 0$; this could be achieved by injecting high-frequency voltage or current signal at low speed and 2) the initial value of $\Delta\theta(k)$ is sufficiently close to $\tilde{\theta}(k)$, which is met when the PLL converges.

C. Sampling Noise Sensitivity

In practice, noises are brought into the variable $\hat{u}_d$, $\hat{u}_q$, $\hat{i}_d$, and $\hat{i}_q$ by current sampling and PWM generation. According to (1), the current noises will eventually reflect on the voltage. A lumped noise voltage $u_{ndq} = [u_{nd} \; u_{nq}]^T$ is used to represent the overall sampling noise. Then, the Taylor expansion of $F(k)$ considering noise is expressed as

$$F \approx \begin{bmatrix} u_{nd} \\ u_{nq} \end{bmatrix} + A\left(\tilde{\theta}(k)\right)\left(\Delta\theta(k) - \tilde{\theta}(k)\right). \tag{18}$$

Based on (18), the position estimation error is derived as

$$\Delta\theta(k) - \tilde{\theta}(k) \approx -\frac{\left[u_{nd} \; u_{nq}\right] A\left(\tilde{\theta}(k)\right)}{\left\| A\left(\tilde{\theta}(k)\right) \right\|^2}. \tag{19}$$

1) Zero Speed: At standstill, the terms associated with ω_e are zero. Error in the estimated position introduced by the noise is

$$\Delta\theta(k) - \tilde{\theta}(k) \approx \frac{\left\| u_{ndq} \right\|}{2L_2 \left\| \Delta\hat{i}_{dq}(k) \right\|/T} \cos\left(2\tilde{\theta}(k) + \psi_n\right) \tag{20}$$

where ψ_n is the phase caused by sampling noise, and it is random if the noise is random. It is shown that the error is dependent on several items. Larger L_2 and $\|\Delta\hat{i}_{dq}(k)\|$ help reduce the error. The sampling noise amplitude $\|u_{ndq}\|$ should be kept at a low level to minimize the error.

2) Medium and High Speeds: The voltage drop caused by L_2 is trivial at medium and high speeds compared to the back EMF, and the terms associated with L_2 are neglected. The error introduced is then derived as

$$\Delta\theta(k) - \tilde{\theta}(k) \approx \frac{\|u_{ndq}\| \cos(\tilde{\theta}(k) + \psi_n)}{\omega_e \psi_f}. \tag{21}$$

According to (21), the amplitude of noise level is directly related to the estimation error; therefore, it should be reduced as much as possible. The estimation error gets reduced as the back EMF gets larger. This indicates the estimation is less noise prone at higher speed.

It should be noted that the estimation error caused by noises is random, and its frequency is as high as the sampling frequency. Therefore, the estimation error caused by sampling will be significantly attenuated after going through the PLL observer.

D. High-Frequency Signal Injection at Standstill to Low Speed

According to (21), the sampling noise will cause larger position estimation error at standstill to low speed because of the low back EMF. The position estimation algorithm will fail if the error becomes too large. As can be seen from (19), the error is reduced by keeping $\|A(\tilde{\theta}(k))\|$ as high as possible. High-frequency signal injection can be used to achieve this goal. At low speed, since both ω_e and L_2 are small, $L_2\omega_e(k)$ is neglected. $\|A(\tilde{\theta}(k))\|^2$ is reformulated as

$$\|A(\tilde{\theta}(k))\|^2 \approx 4L_2^2 \frac{\|\Delta\hat{i}_{dq}(k)\|^2}{T^2} + \omega_e^2 \psi_f^2$$
$$+ \frac{4L_2\omega_e\psi_f}{T} \Delta\hat{i}_{dq}(k)^T \begin{bmatrix} \sin(\tilde{\theta}(k)) \\ -\cos(\tilde{\theta}(k)) \end{bmatrix}. \tag{22}$$

If the position estimation algorithm does not fail, $\tilde{\theta}(k)$ will be very close to zero. Therefore, (22) becomes

$$\|A(\tilde{\theta}(k))\|^2 \approx \frac{4L_2^2}{T^2}(\Delta\hat{i}_d(k)^2 + \Delta\hat{i}_q(k)^2)$$
$$+ \omega_e^2 \psi_f^2 - \frac{4L_2\omega_e\psi_f}{T} \Delta\hat{i}_q(k). \tag{23}$$

It is shown that the value of $\|A(\tilde{\theta}(k))\|^2$ is determined by the variation of $\hat{i}_d$ and $\hat{i}_q$. In actual applications, $\Delta\hat{i}_q(k)$ in each sampling period is small because the sampling frequency is high. Therefore, the terms associated with $\Delta\hat{i}_q(k)$ are neglected. Thus, (23) becomes

$$\|A(\tilde{\theta}(k))\|^2 \approx \frac{4L_2^2}{T^2} \Delta\hat{i}_d(k)^2 + \omega_e^2 \psi_f^2. \tag{24}$$

It is clear that, in order to keep the value of $\|A(\tilde{\theta}(k))\|^2$ high with any ω_e, the term $\Delta\hat{i}_d$ is needed to be none zero when ω_e is small. Thus, high-frequency signal injection should be applied at low speed.

There are several types of high-frequency signals used for injection. The most commonly used one is the sinusoidal signal. However, if sinusoidal signal is used, $\Delta\hat{i}_d(k)$ will become

$$\Delta\hat{i}_d(k) = A\cos(\omega_h t) \tag{25}$$

where A is the amplitude of the injection current and ω_h is the angular speed of the high-frequency signal. According to (25), $\Delta\hat{i}_d(k)$ will be zero at some point ($\omega_h t = pi/2 + Npi$, $N =, \pm1, \pm2, \ldots$). Thus, in order to keep $\|A(\tilde{\theta}(k))\|$ nonzero all the time, square wave or triangular wave signal should be injected instead of the sinusoidal signal. The injected signal is defined as

$$\Delta\hat{i}_d(k) = \pm I_H \tag{26}$$

where I_H is the peak-to-peak value of the injected current. This injected current signal could be generated by applying an additional high-frequency voltage alternating u_H on the voltage reference in the estimated d-axis

$$u_H = \pm L_d \frac{2I_H}{T}. \tag{27}$$

It has to be noted that the injected voltage is a square wave, and the actual caused high-frequency current is a triangular wave. However, in order to keep the injected current as low as possible, the sign of the injected voltage is recommended to alternate every sampling period. In this case, the injected current frequency is half of the sampling frequency, and the sampled current in the controller is still a square wave.

Then, (24) becomes

$$\|A(\tilde{\theta}(k))\|^2 \approx \frac{4L_2^2 I_H^2}{T^2} + \omega_e^2 \psi_f^2. \tag{28}$$

Compared to (15), through injection of high-frequency square wave signal, $\|A(\tilde{\theta}(k))\|^2$ is kept none zero with any ω_e.

E. Parameter Sensitivity

The proposed position estimated method relies on the accurate voltage equation of the motor. However, in practical implementation, the motor parameters in the digital controller might be different from those of the real motor. Therefore, a parameter sensitivity study is carried out.

1) Zero and Low Speed: To simplify the analysis, it is assumed that $I_d = 0$ control is adopted at standstill and low speed. Thus, there is

$$\Delta\hat{i}_d(k) = \pm I_H$$
$$\hat{i}_d(k) = \frac{\pm I_H}{2}. \tag{29}$$

Mismatch in L_2:

First, L_1 is assumed to be accurate, and there is only mismatch in L_2. Neglecting small terms, the position estimation could be approximated by

$$\Delta\theta(k) - \tilde{\theta}(k) \approx \pm \frac{\psi_f \omega_e \tilde{L}_2 T}{4(L_2 + \tilde{L}_2)^2 I_H} \tag{30}$$

where $\tilde{L}_2$ denotes the mismatch in L_2. As can be seen from (30), the error is proportional to $\tilde{L}_2$ and the speed.

Moreover, the error alternates between positive and negative. Therefore, it can be significantly attenuated by the PLL observer.

Mismatch in L_1:

Then, L_2 is assumed to be accurate, and there is only mismatch in L_1. By neglecting small terms and positive–negative alternating terms, the error is approximated by

$$\Delta\theta(k) - \tilde{\theta}(k) \approx \frac{-L_2 \frac{I_H^2}{T}\omega_e\tilde{L}_1 - \psi_f\tilde{L}_1\hat{i}_q\omega_e^2}{4L_2^2\frac{I_H^2}{T^2} + \psi_f^2\omega_e^2} \qquad (31)$$

where $\tilde{L}_1$ denotes the mismatch L_1. It can be seen that the error is proportional to $\tilde{L}_1$. Therefore, $\tilde{L}_1$ should be reduced as much as possible.

Mismatch in R_s:

If there is mismatch in R_s, by neglecting small terms, there is only positive–negative alternating terms left in the position estimation error

$$\Delta\theta(k) - \tilde{\theta}(k) = \frac{\pm\frac{I_H}{T}\tilde{R}\left(-2L_2\hat{i}_q + \frac{\psi_f\omega_e}{2}\right)}{4L_2^2\frac{I_H^2}{T^2} + \psi_f^2\omega_e^2} \qquad (32)$$

where $\tilde{R}$ denotes the mismatch in R_s. Apparently, the error is proportional to $\tilde{R}$ and $\hat{i}_q$. Since the error is alternating between positive and negative, it is also significantly attenuated after going through the PLL.

2) High Speed: When the speed is high, terms associated with L_2 are relatively trivial and are neglected. The effect of the difference between ω_e and $\hat{\omega}_e$ is studied. If $\hat{\omega}_e$ could not track ω_e accurately, $G(k)$ will become

$$G(k) = \psi_f^2(\omega + \tilde{\omega})^2\left(\Delta\theta(k) - \tilde{\theta}(k)\right)^2 + \psi_f^2\tilde{\omega}^2. \qquad (33)$$

Equation (33) indicates that $G(k)$ will not reach zero if ω_e and $\hat{\omega}_e$ are different. However, the solution of $\Delta\theta(k)$ is still $\tilde{\theta}(k)$. Therefore, no error is introduced in the high-speed case.

IV. SOLVING THE OPTIMIZATION PROBLEM

Since at least local convexity of $G(k)$ near $\tilde{\theta}(k)$ in any situation is guaranteed, (11) could be solved numerically. Conventional Newton or quasi-Newton methods need complex calculation of the second-order derivative, which puts too much burden for the digital controller. A simplified approach based on the Taylor expansion is used in this article to release the computational burden. $F(k)$ in (10) is expanded near zero as

$$F(k) \approx F(k)\big|_{\Delta\theta(k)=0} + \frac{dF(k)}{\Delta\theta(k)}\big|_{\Delta\theta(k)=0}(\Delta\theta(k)) \qquad (34)$$

and

$$\frac{dF(k)}{\Delta\theta(k)}\big|_{\Delta\theta(k)=0} = A(0) = 2\omega_e L_2\begin{bmatrix} 1 & 0 \\ 0 & -1 \end{bmatrix}\begin{bmatrix} \hat{i}_d \\ \hat{i}_q \end{bmatrix}$$
$$- 2L_2\begin{bmatrix} 0 & 1 \\ 1 & 0 \end{bmatrix}\frac{d}{dt}\left(\begin{bmatrix} \hat{i}_d \\ \hat{i}_q \end{bmatrix}\right) + \psi_f\omega_e\begin{bmatrix} 1 \\ 0 \end{bmatrix}. \qquad (35)$$

Since $G(k) = F(k)^T F(k)$, the solution of $\Delta\theta(k)$ is obtained as

$$\Delta\theta(k) = -\frac{A(0)^T F(k)\big|_{\Delta\theta(k)=0}}{A(0)^T A(0)}. \qquad (36)$$
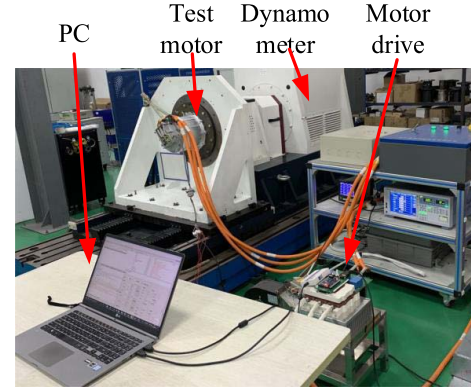

Fig. 5. Experimental setup based on a traction motor.

TABLE I
KEY PARAMETERS OF THE MOTOR AND MOTOR DRIVE

Symbol	Parameter Name	Parameter Value
R_s	Stator resistance	0.044 Ω
L_d	d-axis inductance	500 μH
L_q	q-axis inductance	1100 μH
ψ_f	PM flux linkage	0.054 Wb
p	Number of pole pairs	4
f_s	Sampling frequency	10 kHz
T	Sampling time	0.0001 s
U_{DC}	DC bus voltage	300 V

According to the discussion above, $A(0) > 0$ always holds because of high-frequency signal injection. Therefore, the solution of $\Delta\theta(k)$ is always obtained with less numerical error.

After several iterations to solve (11), the final estimation rotor position at the current sampling period is obtained. According to (34), the value of G is approximated by the Taylor expansion with $\Delta\theta(k) = 0$; therefore, no trigonometric function is needed in the calculation expect calculating $\hat{u}_d$, $\hat{u}_q$, $\hat{i}_d$, and $\hat{i}_q$. The computation cost is significantly reduced. Since, when $\Delta\theta(k)$ is small, according to Fig. 4, the estimated G is very close to the analytical value of G, therefore, few iterations are needed to get the accurate estimation result. After obtaining $\Delta\theta(k)$, $\hat{\theta}_e(k)$ is obtained by (12). After going through the PLL observer, the final estimated position $\hat{\theta}_{PLL}(k)$ and speed $\hat{\omega}_e(k)$ are obtained.

V. EXPERIMENTAL VERIFICATION

To validate the proposed position estimation method, experiments are conducted on a traction motor, as shown in Fig. 5. The traction motor is coupled to a dynamometer. Torque control or speed control can be applied by the dynamometer. The test motor is driven by a motor drive, and the position estimation algorithm is implemented in the motor drive. Table I lists key parameters of the motor and the motor drive. The variables in the control and position estimation algorithm are recorded to the RAM of the motor drive and then transferred to the PC. Only two iterations are used in the solving process. The bandwidth of the PLL observer is set to be 50 Hz.

A. Position Estimation at Standstill and Low Speed

At zero to low speed, a square voltage waveform with an amplitude of 25 V and a frequency of 5 kHz is injected
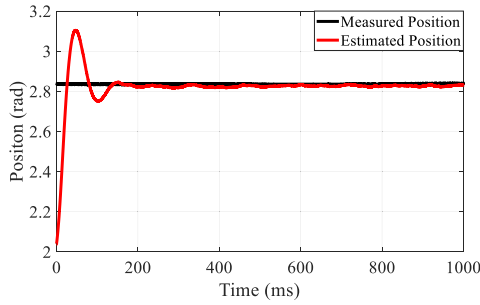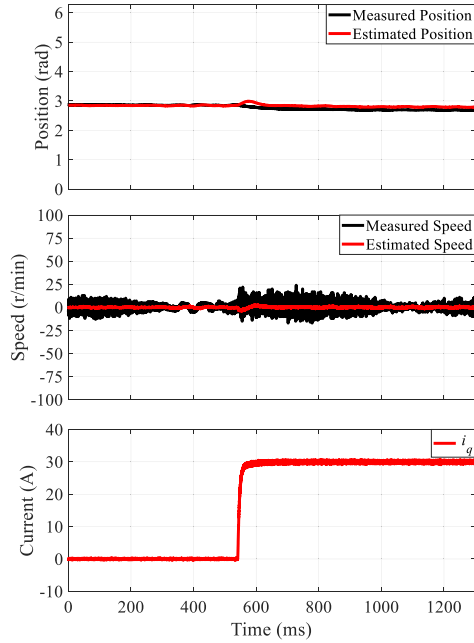
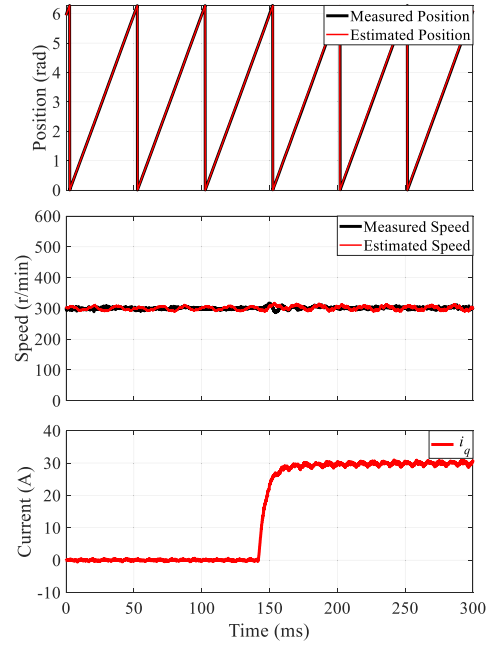Fig. 6. Estimated and measured positions at starting up.

Fig. 7. Measured and estimated positions, speeds, and q-axis current at 0 rpm.

Fig. 8. Measured and estimated positions, speeds, and q-axis current at 300 rpm.

into the stator as a high-frequency signal to estimate the position. This high-frequency voltage only causes the current ripple with an amplitude of less than 2.5 A in the d-axis. That current ripple is relatively small for the test motor. However, it is sufficiently larger than the current sampling noise; therefore, the estimation error caused by the current sampling is limited. The high-frequency current ripple does cause acoustic noise. The noise level measured 1.0 m from the test motor at standstill rises from 52 to 56 dB(A); the noise increase is small and acceptable for traction applications. Several experiments, including starting and load applying, are performed at standstill and low speed.

The positions obtained from estimation and measurements during starting up are compared in Fig. 6. It has to be noted that a normal polarity check is performed before starting up. As can be seen, the estimated position converges swiftly, and little estimation error is observed.

Then, the performance of the proposed method is verified by applying load at constant speed.

Figs. 7 and 8 compare waveforms of the measured position, the estimated position, the measured speed, the estimated

speed, and the q-axis current at 0 and 300 rpm, respectively. As can be seen, the speed and position estimations are accurate even during current transients.

B. Position and Speed Estimation at High Speed

The high-frequency signal injection has to be turned off at high speed. In this test, it is assumed that the voltage noise amplitude $\|u_{ndq}\|$ of the system is limited to 1.5% of U_{dc}, which is relatively easy to be achieved with appropriate compensation. Then, according to (21), in order to limit the maximum estimation error caused by sampling noise within 0.5 rad, the minimum ω_e for high speed is calculated as 166.7 rad/s, which is about 400 rpm. Instead of turning off the high-frequency signal injection immediately, in the test, the injected voltage amplitude starts to decrease linearly when the motor speed exceeds 400 rpm and becomes zero when the motor speed reaches 800 rpm.

Fig. 9 shows waveforms of the measured position, the estimated position, the measured speed, the estimated speed, and the q-axis current at 3000 rpm. It is shown that the speed and position estimations are not affected by the current dynamics.

C. Position and Speed Estimation Under Speed Dynamics

More dynamic tests are performed to verify the performance of the proposed method during speed transients. First, the motor is accelerated from standstill to 5000 rpm with $i_q = 30$ A. The measured and estimated speed, position estimation error, the value of A, and i_q are shown in Fig. 10. It is shown that, during the speed acceleration, the speed estimation is accurate and fast, the estimation error is small, and the value of A is guaranteed to be larger than zero.
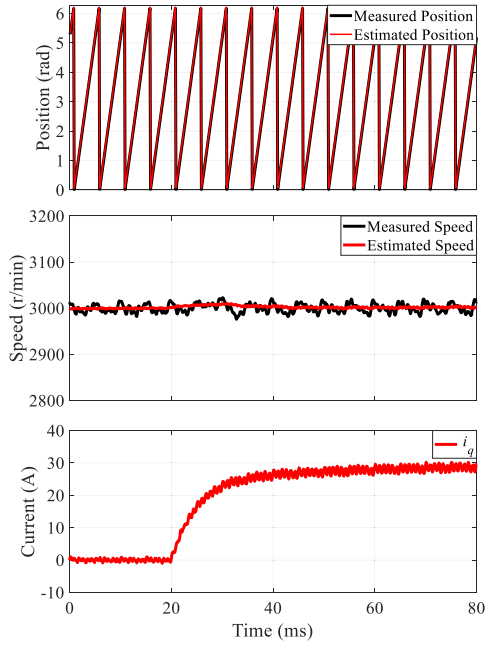
Fig. 9. Measured and estimated positions, speeds, and q-axis current at 3000 rpm.
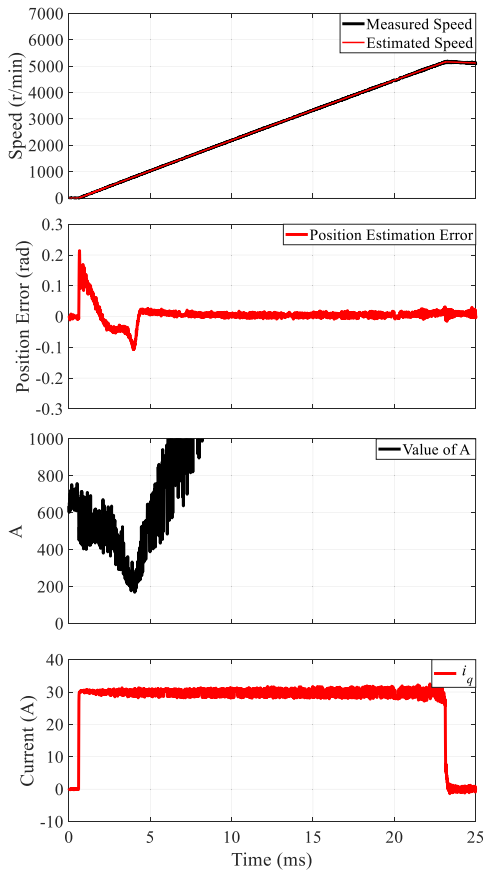

Fig. 10. Measured and estimated positions, estimation error, and A- and q-axis currents during a constant current acceleration.

Another test is performed by accelerating the motor from negative speed to positive speed. i_q changes several times during the acceleration, as presented in Fig. 11. It shows
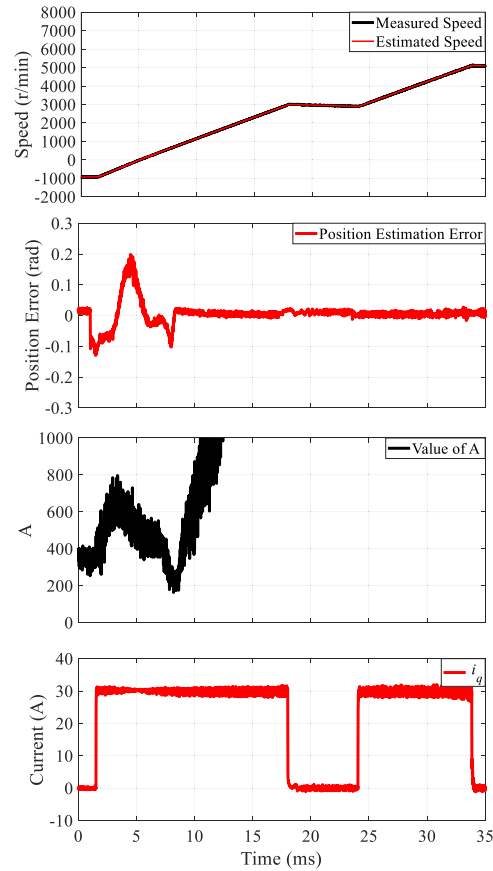

Fig. 11. Measured and estimated positions, estimation error, and A- and q-axis currents during a variable current acceleration.

that the estimated speed tracks the measured speed precisely. The estimation error is limited even during speed or current transients. A is always larger than zero. It has to be noted that the position estimation error is slightly larger at low speed, which can be attributed to the unmodeled cross coupling between the dq-axes. Since the unmodeled mismatch is small, the position estimation error is also limited.

D. Algorithm Computation Time and Injected Voltage Comparison

The proposed position estimation algorithm is implemented with a 300-MHz processor. In the test, two iterations are used to get the estimation results, and the total execution time, including signal sampling, current control, position, and speed estimation, is 30 μs. Compared with the existing optimization-based position estimation method, the algorithm proposed in [27] needs 33 μs to execute with only one iteration on a 900-MHz processor. The method proposed in [29] is also implemented and tested on the 300-MHz processor. Since that method is similar to the proposed method, the execution time is close. That method is a little bit slower than the method proposed in this article, but that proposed method is less complex for analysis compared to that method. With the same dc bus voltage, the injected voltages in this test and in [29] are both square waves with a 25-V amplitude and a 5-kHz frequency. The injected voltage is much smaller than that used

TABLE II
BRIEF COMPARISON WITH EXISTING OPTIMIZATION-BASED POSITION ESTIMATION METHOD

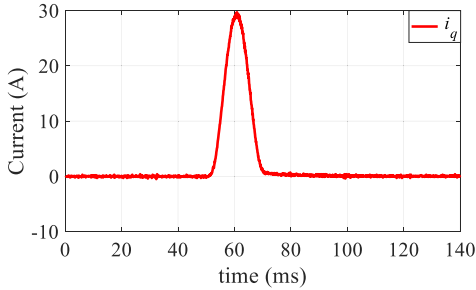| Method	Processor	Execution time	Injected voltage signal	Injected voltage amplitude and frequency	Injection stop speed
Proposed	300 Mhz	30 us (2 iterations)	Square wave	25 V with 300 V U_{DC}, 5k Hz	800 r/min
in [27]	900 Mhz	33 us (1 iteration)	Sinusoidal wave	75 V with 300 V U_{DC}, 500 Hz	400 r/min
in [29]	300 Mhz	31 us (2 iterations)	Square wave	25 V with 300 V U_{DC}, 5k Hz	425 r/min

Fig. 12.   Current pulse in the q-axis for parameter mismatch tests.
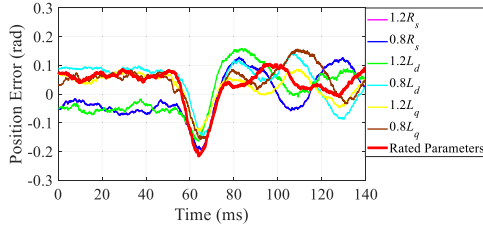
Fig. 13.   Recorded position estimation errors under parameter mismatch tests at zero speed.

Fig. 14.   Recorded position estimation errors under parameter mismatch tests at 3000 rpm.

in [27]. A brief summary of the algorithm computation burden and the injection voltage of the recent optimization-based position estimation method is shown in Table II. It is shown that the computation burden of the proposed position estimation algorithm is significantly reduced. Therefore, the cheaper microprocessor could be selected to reduce the system cost.

E. Parameter Sensitivity Test

The parameter mismatch between the real motor and motor drive exists in real applications. Experiments are conducted to test the parameter sensitivity of the proposed position estimation method. Two tests are performed.

First, at zero speed, the parameters R_s, L_d, and L_q in the controller change from -20% to $+20\%$ of their rated values, respectively. A current pulse of 30 A in the q-axis is applied, as shown in Fig. 12. The position estimation errors under these cases are shown in Fig. 13. At zero speed, the high-frequency signal injection is active, it is shown that the position estimation errors under these parameter mismatch cases are similar, and no obvious error is caused.

Second, at 3000 rpm, the parameters R_s, L_d, L_q, and ψ_f in the controller are changed from -20% to $+20\%$ of their rated values, respectively. The same current pulse, as shown in Fig. 12, is applied. The Position estimation errors under these mismatch cases are shown in Fig. 14. It is shown that, compared with the position estimation error with rated
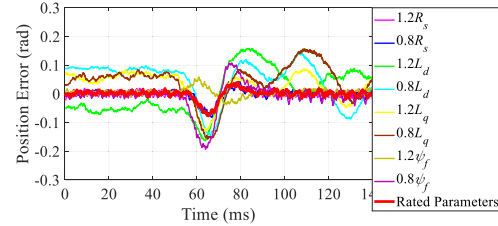
parameters, mismatched parameters, such as L_d, L_q, and ψ_f, do cause additional estimation errors. However, these error are small and limited.

The above tests at low speed and high speed indicate that the proposed position estimation method has sufficient robustness for parameter mismatch.

VI. CONCLUSION

This article proposed a full-speed range rotor position and speed estimation method for IPMSM in the synchronous rotating frame. A single-variable optimization problem has been formulated to solve the rotor position at the current sampling steps. The solved position is fed into a PLL observer to get the estimated rotor speed and smooth out the estimated rotor position. The convexity of the optimization problem, the effects of sampling noise, and the parameter mismatch are analyzed. By formulating and analyzing the optimization in the synchronous frame, the derivation and solving process are more simplified. Finally, experiments are conducted in both steady and dynamic situation to validate the proposed optimization-based position and speed estimation method. The proposed algorithm can obtain the estimated rotor position and speed with high accuracy throughout the whole speed range, as shown in the experiments. The robustness for parameter mismatch is also verified by experiments. Since a less trigonometric function is required, the computational cost and complexity are significantly reduced compared to existing optimization-based methods.

REFERENCES

[1] D. Xu, B. Wang, G. Zhang, G. Wang, and Y. Yu, "A review of sensorless control methods for AC motor drives," *CES Trans. Electr. Mach. Syst.*, vol. 2, no. 1, pp. 104–115, Mar. 2018.

[2] N. K. Quang, N. T. Hieu, and Q. P. Ha, "FPGA-based sensorless PMSM speed control using reduced-order extended Kalman filters," *IEEE Trans. Ind. Electron.*, vol. 61, no. 12, pp. 6574–6582, Dec. 2014.

[3] E.-K. Kim, J. Kim, H. T. Nguyen, H. H. Choi, and J.-W. Jung, "Compensation of parameter uncertainty using an adaptive sliding mode control strategy for an interior permanent magnet synchronous motor drive," *IEEE Access*, vol. 7, pp. 11913–11923, 2019.

[4] C. Shi, J. Luo, J. Huang, Z. Yu, and C. Wen, "New sensorless control for interior permanent magnet synchronous motors of electric vehicle," in *Proc. 2nd IEEE Conf. Energy Internet Energy Syst. Integr. (EI)*, Oct. 2018, pp. 1–5.

[5] X. Liu, H. Yu, J. Yu, and L. Zhao, "Combined speed and current terminal sliding mode control with nonlinear disturbance observer for PMSM drive," *IEEE Access*, vol. 6, pp. 29594–29601, 2018.

[6] H. Kim, K.-K. Huh, R. D. Lorenz, and T. M. Jahns, "A novel method for initial rotor position estimation for IPM synchronous machine drives," *IEEE Trans. Ind. Appl.*, vol. 40, no. 5, pp. 1369–1378, Sep. 2004.

[7] J. M. Guerrero, M. Leetmaa, F. Briz, A. Zamarron, and R. D. Lorenz, "Inverter nonlinearity effects in high-frequency signal-injection-based sensorless control methods," *IEEE Trans. Ind. Appl.*, vol. 41, no. 2, pp. 618–626, Mar. 2005.

[8] G. Foo, S. Sayeef, and M. F. Rahman, "Sensorless direct torque and flux control of an IPM synchronous motor at low speed and standstill," in *Proc. 13th Int. Power Electron. Motion Control Conf.*, Sep. 2008, pp. 2269–2274.

[9] G. Foo and M. F. Rahman, "Sensorless sliding-mode MTPA control of an IPM synchronous motor drive using a sliding-mode observer and HF signal injection," *IEEE Trans. Ind. Electron.*, vol. 57, no. 4, pp. 1270–1278, Apr. 2010.

[10] D. Raca, P. Garcia, D. D. Reigosa, F. Briz, and R. D. Lorenz, "Carrier-signal selection for sensorless control of PM synchronous machines at zero and very low speeds," *IEEE Trans. Ind. Appl.*, vol. 46, no. 1, pp. 167–178, Jan. 2010.

[11] G. Bisheimer, M. Sonnaillon, C. D. Angelo, J. Solsona, and G. Garcia, "Full speed range permanent magnet synchronous motor control without mechanical sensors," *IET Electr. Power Appl.*, vol. 4, no. 1, pp. 35–44, Jan. 2010.

[12] A. Accetta, M. Cirrincione, M. Pucci, and G. Vitale, "Sensorless control of PMSM fractional horsepower drives by signal injection and neural adaptive-band filtering," *IEEE Trans. Ind. Electron.*, vol. 59, no. 3, pp. 1355–1366, Mar. 2012.

[13] G. Wang, R. Yang, and D. Xu, "DSP-based control of sensorless IPMSM drives for wide-speed-range operation," *IEEE Trans. Ind. Electron.*, vol. 60, no. 2, pp. 720–727, Feb. 2013.

[14] J. M. Liu and Z. Q. Zhu, "Novel sensorless control strategy with injection of high-frequency pulsating carrier signal into stationary reference frame," *IEEE Trans. Ind. Appl.*, vol. 50, no. 4, pp. 2574–2583, Jul. 2014.

[15] Y.-C. Kwon, J. Lee, and S.-K. Sul, "Full torque-range low-speed sensorless drive for heavily saturated IPMSMs by manipulation of convergence point," in *Proc. IEEE Energy Convers. Congr. Exposit. (ECCE)*. Cincinnati, OH, USA: IEEE, Oct. 2017, pp. 865–872.

[16] C. You, J. Li, X. Huang, Y. Fang, and J. Ma, "A full-speed sensorless control algorithm for interior permanent magnet synchronous motor using sliding-mode observer and HF signal injection," in *Proc. IEEE Vehicle Power Propuls. Conf. (VPPC)*. Belfort, CA, USA: IEEE, Dec. 2017, pp. 1–6.

[17] H. Li, X. Zhang, C. Xu, and J. Hong, "Sensorless control of IPMSM using moving-average-filter based PLL on HF pulsating signal injection method," *IEEE Trans. Energy Convers.*, vol. 35, no. 1, pp. 43–52, Mar. 2020.

[18] M. X. Bui, D. Q. Guan, D. Xiao, and M. F. Rahman, "Sensorless control of interior permanent magnet synchronous motor based on the fundamental pulse width modulation excitation over a wide speed range," in *Proc. 19th Int. Conf. Elect. Mach. Syst. (ICEMS)*, 2016, pp. 1–6.

[19] M. X. Bui, M. F. Rahman, and D. Xiao, "Sensorless control of interior permanent magnet synchronous machines based on the combination of the modified FPE method and SMO," in *Proc. IEEE 9th Int. Symp. Sensorless Control Electr. Drives (SLED)*. Helsinki, Finland: IEEE, Sep. 2018, pp. 126–131.

[20] M. X. Bui, M. F. Rahman, and D. Xiao, "Hybrid sensorless control of an interior permanent magnet synchronous machine using current derivative measurements and a sliding mode observer," in *Proc. IEEE Energy Convers. Congr. Expo. (ECCE)*. Portland, OR, USA: IEEE, Sep. 2018, pp. 344–351.

[21] M. X. Bui, D. Guan, D. Xiao, and M. F. Rahman, "A modified sensorless control scheme for interior permanent magnet synchronous motor over zero to rated speed range using current derivative measurements," *IEEE Trans. Ind. Electron.*, vol. 66, no. 1, pp. 102–113, Jan. 2019.

[22] M. X. Bui, M. F. Rahman, and D. Xiao, "A hybrid sensorless controller of an interior permanent magnet synchronous machine using current derivative measurements and a sliding mode observer," *IEEE Trans. Ind. Appl.*, vol. 56, no. 1, pp. 314–324, Jan. 2020.

[23] S. Nalakath, Y. Sun, M. Preindl, and A. Emadi, "Optimization-based position sensorless finite control set model predictive control for IPMSMs," *IEEE Trans. Power Electron.*, vol. 33, no. 10, pp. 8672–8682, Oct. 2018.

[24] W. T. Villet, M. J. Kamper, P. Landsmann, and R. Kennel, "Hybrid position sensorless vector control of a reluctance synchronous machine through the entire speed range," in *Proc. 15th Int. Power Electron. Motion Control Conf. (EPE/PEMC)*, Sep. 2012. pp. LS4b-1.1-1–LS4b-1.1-7.

[25] D. O. Kisck, D. Anghel, M. Kisck, and J. W. Kim, "Study and implementation of sensorless speed control of interior permanent magnet motor from zero to very high speed," in *Proc. 40th Annu. Conf. IEEE Ind. Electron. Soc. (IECON)*. Dallas, TX, USA: IEEE, Oct. 2014, pp. 912–918.

[26] J. Choi, K. Nam, A. A. Bobtsov, and R. Ortega, "Sensorless control of IPMSM based on regression model," *IEEE Trans. Power Electron.*, vol. 34, no. 9, pp. 9191–9201, Sep. 2019.

[27] Y. Sun, M. Preindl, S. Sirouspour, and A. Emadi, "Unified wide-speed sensorless scheme using nonlinear optimization for IPMSM drives," *IEEE Trans. Power Electron.*, vol. 32, no. 8, pp. 6308–6322, Aug. 2017.

[28] Z. Wang, B. Xie, L. Bu, W. Liu, F. Peng, and Y. Huang, "Position sensorless control of IPMSM based on quasi-Newton methods," in *Proc. 22nd Int. Conf. Electr. Mach. Syst. (ICEMS)*, Aug. 2019, pp. 1–6.

[29] F. Peng, Y. Yao, Z. Wang, Y. Huang, H. Yang, and B. Xie, "Position estimation method of IPMSM in full speed range by simplified quadratic optimization," *IEEE Access*, vol. 8, pp. 109964–109975, 2020.
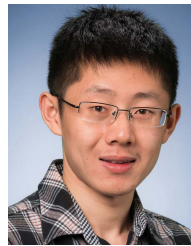
Fei Peng (Member, IEEE) received the B.S. and M.S. degrees in electrical engineering from Southeast University, Nanjing, China, in 2010 and 2012, respectively, and the Ph.D. degree from McMaster University, Hamilton, ON, Canada, in 2016.

He worked as a Post-Doctoral Fellow with the McMaster Institute for Automotive Research and Technology (MacAUTO), McMaster University. From December 2016, he joined the School of Electrical Engineering, Southeast University, Nanjing, China, as an Assistant Professor. His current research interests include optimal design and control of power converters and modeling and digital control of motor drives.
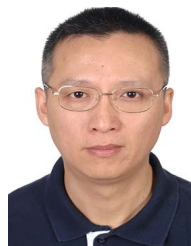
Zhi Cao (Student Member, IEEE) received the B.S. degree in electrical engineering from Southeast University, Nanjing, China, in 2016, where he is currently pursuing the doctor of engineering degree in electric machines and control with the School of Electrical Engineering.

His main research interests include the design, analysis, and control of active magnetic bearing systems.

Jianning Dong (Member, IEEE) received the B.S. and Ph.D. degrees in electrical engineering from Southeast University, Nanjing, China, in 2010 and 2015, respectively.

He was a Post-Doctoral Researcher with the McMaster Automotive Resource Center, McMaster University, Hamilton, ON, Canada. Since 2016, he has been an Assistant Professor with the Delft University of Technology, Delft, The Netherlands. His current research interests include the design, modeling, and control of electromechanical systems and wireless power transfer.

Yunkai Huang (Member, IEEE) received the M.Sc. and Ph.D. degrees in electrical engineering from Southeast University, Nanjing, China, in 2001 and 2007, respectively.

He is currently a Professor with the School of Electrical Engineering, Southeast University. His current research interests include design and control of permanent magnet (PM) machine and high-speed machine, applications in domestic appliances, electric vehicles, railway traction, all-electric ships, more-electric aircraft, and wind power generation systems.